Classical analogue of an interstellar travel through a hydrodynamic wormhole

L.-P. Euvé and G. Rousseaux

Institut Pprime, UPR 3346, CNRS-Université de Poitiers-ISAE ENSMA,
11 Boulevard Marie et Pierre Curie-Téléport 2, B.P. 30179,
86962 Futuroscope Cedex, France

The classical theory of space-time, namely general relativity, suggests but does not demonstrate the existence of so-called wormholes allowing for interstellar journeys. Alternative proposals such as quantum gravity theories are developed nowadays to allow for wormhole travels by assuming hypothetical trans-Planckian effects at tiny scales. Here we show experimentally that analogue traversable and bidirectional wormholes exist in hydrodynamics following a suggestion by Wheeler. Using a water channel, we sent free surface waves on a countercurrent in an analogue gravity setup aiming at showing that hydrodynamic wormhole travels are controlled by a cascade of dispersive scales including surface tension effects: the capillary wavelength plays the role of a Planckian scale below which long gravity waves are transformed into short capillary waves that are able to move at speeds higher than the "flow" of space-time. Whereas our results do not apply to putative astrophysical wormholes *per se*, we anticipate that they will trigger new ideas to explore quantum gravity physics.

I. INTRODUCTION

The point singularity at the heart of models of black holes like the 1916 Schwarzschild-Droste solution of Einstein's theory of general relativity leads to the failure of providing a complete history for the geodesics of massless and massive particles encountering the singularity [1,2]. In 1935, Einstein and Rosen tried to link two external solutions *à la* Schwarzschild by "a bridge" whose interior solution was geodesically incomplete [3]. In 1959, Fronsdal and separately Kruskal in 1960 designed an analytic extension of the Schwarzschild solution by coupling a black hole with its time-reversed solution (a white hole spewing rather than swallowing matter, a solution discovered by Flamm in 1916 [4]) forming a so-called "wormhole" [5,6] (a term coined by Wheeler in 1957 for a tunnel-like shortcut through space-time [7–10]) which closed too rapidly for light to travel inside. In 1973, Ellis found a way to force the Schwarzschild singularity to stay open by replacing it by a "drain hole" with a vector field on the associated space-time which can be interpreted as a velocity field for an "aether" draining through the hole [11]. In order to achieve this "plumbing" device, Ellis coupled Einstein's vacuum field equations with a scalar field in order to open the point singularity. As Ellis imagined, the aether "is more than a mere inert medium for the propagation of electromagnetic waves; it is a restless, flowing continuum whose internal, relative motions manifest themselves to us as gravity. Mass particles appear as sinks or sources of this flowing ether." Ellis introduced a drain hole line element with a coordinate three speed [11]. During the 1970s and independently,

White [12], Anderson and Spiegel [13] and Unruh [14] developed the so-called "rimfall" analogy between the propagation of light in a curved space-time and the way waves propagate on a moving medium [15–18]. For example, White derived the "acoustic" metric in 1971 with a velocity of the moving medium akin to Ellis' aether flow. In 1975, Anderson and Spiegel thought that waves propagating in a moving medium could be kinematically trapped, paving the way to the seminal paper of Unruh in 1981 where he envisaged the possibility to observe in laboratory experiments the Hawking radiation emanating from an analogue black hole horizon, namely the kinematical amplification of quantum vacuum fluctuations by the tidal forces mimicked by the flow gradient at the analogue horizon [19]. Unruh's analogy when applied to condensed matter systems solves two difficulties with Hawking's prediction: firstly, the outgoing radiation appears to originate from arbitrarily short wavelengths in the vicinity of the horizon; secondly, the corresponding energy of the fluctuations goes to infinity transforming the horizon into a caustic. The so-called trans-Planckian problem related to the wavelength was tackled by Jacobson in 1991 who suggested that dispersion would avoid the infinite blue-shifting to the detriment of Lorenz invariance of the theory [20–22]: analogue condensed matter systems are naturally dispersive and/or dissipative at small scales. Hence, they make perfect systems in order to test the Hawking prediction and its robustness even in the presence of dispersion: analogue gravity was born [15–18]. The notion of an event horizon is extended by the notion of a dispersive group velocity horizon or turning point which can be computed from extrema of the dispersion relation.

Quite separately, theories of quantum gravity like rainbow gravity were developed allowing Lorentz symmetry breaking (see a modern discussion in [23]) following another suggestion of Wheeler known as the "quantum foam" [7–10]. Indeed, during the 1960s, he considered wormholes as ultramicroscopic objects (Planck-scale sized) forming a quantum foam connecting separate regions of space-time. He compared the situation to the free surface of ocean which looks flat from an airplane view but who becomes choppy when approaching the surface. The wave turbulence properties of space-time would be controlled by Planckian units that Wheeler was again the first to discuss in an astrophysical context [7–10]. Taking seriously the paradigms of modified gravity like rainbow gravity [23] or analogue gravity [15–18], it turns out that dispersive effects at the Planck scale may control the physics of wormhole travel. According to Wheeler [8], "obviously there is no reason to expect any direct analogy between collective disturbances in the Einstein-Maxwell field and those that take place in a crystal lattice. Let it nevertheless be insisted that one shall leave no stone unturned in searching for special phenomena associated with the propagation of energy through space… Disturbances of very short wavelength will feel out the microcurvature of space and will not propagate normally. The same will be true of disturbances of very long wavelength, comparable to the radius of the Universe. Consequently a disturbance that is originally localized will be dispersed. However, if the dispersion curve possesses a point of inflection, then disturbances made out of wavelengths near the point of inflection will keep together for a long time in the linear approximation."

Recently, Hawking claimed that the strict notion of an "event horizon" was incompatible with quantum mechanics since according to him "there is no escape from a black hole in classical theory, but quantum theory enables energy and information to escape" [24]. Wheeler's guess and Hawking's conjecture (*"there are no black holes"*) are supported by analogue gravity. Indeed, high- and low-energy behavior in a condensed matter system display departures from the linear dispersion relation. For example, a Bose-Einstein condensate features a superluminal correction in the Bogoliubov dispersion relation whereas water waves can display either subluminal, superluminal or inflectional behavior *à la* Wheeler depending on the physical parameters [18]. These corrections to the linear dispersion relation are controlled by the inclusion of microscopic dispersive scales in the system reminiscent of the Planck scale: the healing length in a Bose-Einstein condensate, the water depth or the capillary wavelength in water waves. Hence, one concludes that there are no analogue black holes because of dispersion in condensed matter systems. Hawking suggested the possibility of a so-called "apparent horizon" in addition to the event horizon; the former is a frontier region where the light rays would be suspended when trying to escape from the black hole [24].

In this work, we use water waves for a condensed matter system amenable to experiments as described in [25–38]. In the long-wavelength limit, both systems in general relativity and condensed matter physics are described by the following effective metric: $ds^2 = c^2 dt^2 - (dx - U dt)^2$. For surface waves, they propagate in the same way as a massless scalar field [25]. When the analogy is broken (by "entering the white hole" and "escaping from the black hole"), it is principally through the short-wavelength dispersive effects [25–37] which already breaks the exactness of the mapping to an effective metric [21,22]. The effective $1 + 1$ dimensional metric is expressed in terms of both flow velocity $U(x)$ and wave speed $c(x)$ profiles that can both be tuned experimentally. One recalls that in general relativity, c is constant whereas it is often space dependent in condensed matter setups. In our experiment, both profiles are given by the geometry of the obstacle used to change the water depth. It is also of course important that this metric is only correct in the dispersionless case, whereas our experiment relies on dispersion.

The inflectional behavior of the water wave dispersion relation will allow us to prove experimentally, after our theoretical and numerical predictions, that analogue wormhole travels in hydraulic settings are controlled by a cascade of dispersive effects, one of which, the one associated to the capillary length, could be an analogue candidate for a quantum gravity behavior. To the best of our knowledge, this is the first experiment in the field of analogue gravity to demonstrate the existence of an analogue wormhole travel following our theoretical and numerical predictions [36]. Sabin has discussed recently another proposal in the context of a dc-SQUID array [39]. We will base ourselves on the concept of a *Wheeler wormhole*, a wormhole featuring dispersive horizons (analogous to the event and apparent horizons *à la* Hawking) whose bidirectionality is controlled by microphysical effects. In astrophysics, microphysical effects would correspond to trans-Planckian physics and possibly quantum gravity regimes. In hydrodynamics, microphysical effects correspond to surface tension physics. Other types of wormholes without a horizon like the Morris-Thorne wormhole have been proposed in the literature [40–45]. We will show the existence of an analogue Morris-Thorne wormhole as well by playing on the physical parameters of our experiments: hence, traversability is not necessarily a synonym of the absence of horizon. This latter kind of wormhole requires in general relativity the inclusion of either a so-called exotic matter with a nonstandard stress-energy tensor, "phantom energy" or "scalar field" and so on, to stabilize them [5,6]: it is outside the scope of the present paper to understand why, in hydrodynamics, the analogue wormholes are stable. One can simply argue that Navier-Stokes equations are different from Einstein's equations and that stability of the hydraulic wormhole is possibly linked to the fluid dynamics. Constraints on the energy to keep open the wormhole by a "repulsive" gravity [6,45] are certainly

violated at small scales in analogue systems. Besides, the velocity profiles in hydrodynamics do not necessarily have a "central" singularity like in general relativity: for example, the Schwarzschild-Droste solution in Painlevé-Gullstrand coordinates $V(r) = -c\sqrt{r_S/r}$ (where $r_s = 2GM/c^2$ is the Schwarzschild radius) is equivalent to a radial flow which is singular at $r = 0$ [1,2]. The longitudinal speed profile $U(x)$ used in our experiments is regular in the wormhole region defined as the region between a pair of black and white hole horizons. Moreover, our experimental dispersive horizons are eternal since the flow is "pumped" continuously and there is no evaporation of the black or white holes on the time scale of the experiments. Time-dependent flow behavior is outside the scope of the present paper since it will certainly involve the underlying dynamics. As explained in Peloquin *et al.* [36], the direct travel from the black to the white horizon is rather without interest when the flow gradients dU/dx are small: a redshifting of the gravity wave entering the black horizon takes place and so does a blueshifting when getting outside from the white horizon since the wave is propagating in the same direction as the flow current. Here, we will focus on the reverse travel from the white horizon to the black horizon since it will display the effect of small-scale physics controlled by surface tension. The flow speeds are sufficiently small to avoid the appearance of negative energy waves akin to antiparticles. For the same reason, we will not look at a black hole laser effect since it is beyond the main objectives of this paper (see [36] for some numerical simulations). Negative energies are often mentioned to cause light rays to defocus at the throat of the wormhole like in the original proposal by Thorne *et al.* [40,41]: the defocusing is controlled by the underlying dynamics in our work.

II. EXPERIMENTAL SETUP, METROLOGY AND PARAMETER CHOICES

Our experiments were performed in the water channel of the Pprime Institute in Poitiers (see Fig. 1) and were inspired by the previous works [26–29,31–38].

The dimensions of the channel are length × width × height = 6.5m × 0.39m × 0.6 m (Fig. 1). A PCM Moineau pump regulated by a variable frequency drive can reach a maximum flow rate of 65 Ls^{-1}.

The spatially varying background was set up by an obstacle whose geometry $h_B(x)$ is the same as in the Vancouver experiments [29] which is 1.55 m long and 0.106 m high (Fig. 1). The volumetric flow rate is adjusted by a pump at $Q = 8.13$ Ls^{-1} and the asymptotic water depth h_0 is set at 205 mm to get velocities U of the free surface in the range between 0.102 and 0.203 ms^{-1} due to the presence of the bottom obstruction (the Froude number varying between 0.07 and 0.20).

As explained in [28], the maximum velocity must be in the range $[U_c = -0.178...U_\gamma = -0.23]$ ms^{-1} in order not to
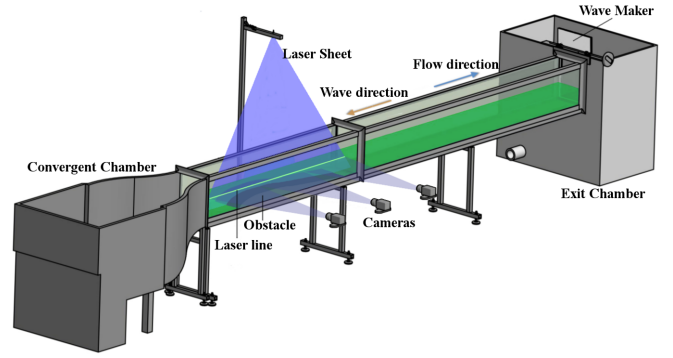

FIG. 1. Scheme of the experimental setup with the water channel with dark green fluorescein, the blue laser sheet with its light green signature on the free surface and the three measurement side cameras.

have extra features well known in analogue gravity such as the appearance of a stationary undulation or negative energy waves with a corresponding black hole laser effect [36]. Figure 2 represents the phase diagram (U, T) indicating where the blocking velocities $|U|$ at which the white ("event"), blue ("apparent") and negative horizons occur, as a function of the wave period T (the procedure to obtain this phase diagram is explained in [28]). The incident period T_I must be less than $2\pi/\omega_{\min}$, to be blocked at the white horizon (the evolution of the frequency $\omega_{\min}$ defined in Fig. 2 as a function of the Froude number and the water depth was studied in [34]) and superior to T_c in order to observe a
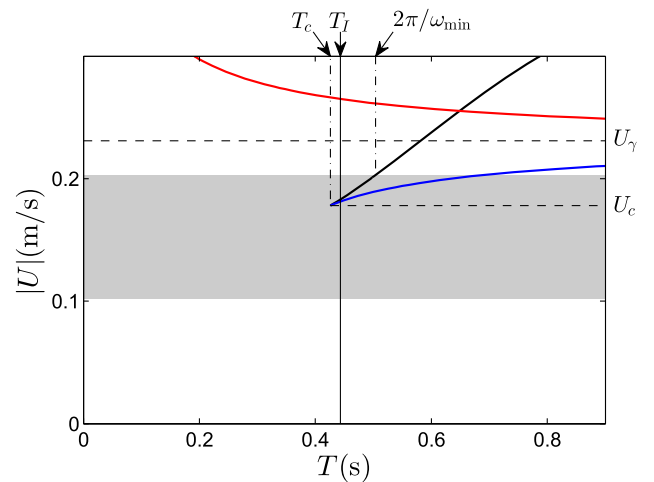

FIG. 2. Phase diagram (U, T). The black, blue and red curves correspond to, respectively, the white, blue and negative horizons. The gray region indicates the velocity range. The horizontal dashed lines correspond to the critical velocity $U_c = -0.178$ ms^{-1} (where the white and blue horizons merge) and $U_\gamma = -0.23$ ms^{-1} the minimum velocity for the appearance of a stationary undulation. The vertical point-dashed lines indicate the critical period T_c and the maximum period for the blocking $2\pi/\omega_{\min}$. The vertical continuous line represents the incident period T_I.

double-bouncing behavior [28]: (T_c, U_c) is the critical point where the white (event) and blue (apparent) horizons merge. So, the period of the incident wave is fixed at $T_c = 0.425$ s $< T_I = 0.443$ s $< 2\pi/\omega_{\min} = 0.504$ s (the related angular frequency satisfying $\omega_c = 14.78$ Hz $> \omega_I = 14.17$ Hz $> \omega_{\min} = 12.47$ Hz).

Thanks to a newly designed wave maker placed at the end of the channel, we create a sinusoidal wave with a very small initial amplitude at the position of the wave maker in order to stay in the linear regime during all the mode conversions. The actual mechanical amplitude of the sinusoidal wave-maker displacement is $a_m = 200~\mu$m and the resulting amplitude of the incoming sinusoidal water wave is $a_0 = 11.53~\mu$m for the incident wave generated in our experiments (see the discussion below for the choice of this amplitude).

To measure the free surface deformations $\delta h(\omega_I, x, t)$ for a fixed angular frequency ω_I as a function of position along the channel x and time t induced by the (reverse) wormhole travel with a good precision, we use several cameras with a total field of vision of roughly 1.1 m wide and a spatial resolution of 0.219 mm per pixel (see Fig. 1). The free surface is probed by a laser-induced fluorescence scanning technique similar to the one discussed in [29,37]. We use a laser diode (MBL-III-473 from Changchun New Industries) with a POWELL lens ($N - SF6, 75°$) to generate a vertical laser sheet impacting the free surface of water in the center of the water channel [37]. Imaging of the fluorescent line delineating the free surface was done with three cameras (Grasshopper 3 CGS3.U3.41C6M from Pointgrey, 2048×2048 pixels with a maximum of 90 frames per second, Nikon objectives 35 mm) and we record movies made of 131072 (2^{17}) images at a rate of 18.02 Hz. A subpixel free surface detection method similar to the one used in [29] allows us to measure waves with amplitudes smaller than 0.1 μm. It is based on laser-induced fluorescence using fluoresceine mixed with water: free surface deformations are visualized by the fluorescent emission of a laser sheet impacting the water surface and exciting the dye. We capture the free surface deformations during 2 hours corresponding to a number of images in powers of 2, namely 2^{17} for an accurate Fourier transform, the acquisition frequency being chosen to have an exact number of periods.

III. EXPERIMENTAL SPACE-TIME DIAGRAMS

In 1977, Basovich and Talanov studied carefully the kinematics of gravity-capillary waves and their transformations on inhomogeneous currents [46] (see the simultaneous theoretical work by Smith in [47]). They looked to the conditions of reflections of wave packets by a countercurrent. A gravity wave opposed to the current was predicted to be shortened (blueshifted using an optical terminology) and blocked when the group velocity cancels at a first turning point known as the wave blocking point (the analogue of a white hole horizon). Then, the

incoming wave is reflected by mode converting into another gravity wave with a shorter wavelength (the so-called blueshifted wave). The latter has positive phase velocity but negative group velocity. Hence, while drifting backward in terms of energy the blueshifted wave shortens. Up to now, this process is controlled by the water depth and the frequency of the incoming waves but does not depend on the surface tension of the fluid. When including the effect of capillarity, the blueshifted waves can be blocked at a second turning point and then mode converted into capillary waves with positive phase and group velocity propagating opposite to the current on the "back" of both the incoming and blueshifted waves. When reaching the first turning point the capillary waves are not blocked contrary to the incident gravity waves. Wavelength shortening and double reflection of gravity-capillary waves on an inhomogeneous current were observed experimentally in the works of Pokazeev and Rozenberg [48] and Badulin, Pokazeev and Rozenberg [49] in 1983. An obstacle was placed on the bottom of the water channel to vary the flow and the associated speed range was between 0.04 and 0.3 m·s^{-1} (speed between 0.04 and 0.21 m·s^{-1} over a sloping bottom in [48] and speeds up to 0.3 m·s^{-1} over a bump obstacle in [49]). The central frequencies of incoming wave packets propagating on the countercurrent were in the range of 1.5–11 Hz with three to ten oscillations within the envelope of the packets (in the range of 2–11 Hz for [48] and in the range 1.5–3 Hz for [49]). A huge decrease of the wavelength was observed e.g. from 20 cm down to 2 mm. The distance between both reflection points was typically of the order of one local wavelength. The transmitted capillary waves were highly dissipated by viscosity on the top of the obstacle in the fastest region of the flow speed and were not seen to reach the other side of the obstacle. It is unclear whether the waves in Badulin, Pokazeev and Rozenberg experiments were damped or if the resolution of the sensors used to measure the wave amplitude was not sufficient small to detect a (reverse) wormhole travel, namely the transmission of gravity waves after their dual mode conversion into capillary waves when propagating above the obstacle [49]. Theoretical and numerical works were subsequently done by Trulsen and Mei in 1993 [50] who added the effect of viscosity which damps the capillary waves during the double bouncing conversion without being able to make quantitative comparisons between theory and experiments because of a lack of data: we intend to fill this gap in this paper.

In the linear regime where the frequency is conserved, the ray trajectories are described by the ray theory using Hamilton equations $dk/dt = -\partial\omega/\partial x = -kdU/dx$, $dx/dt = \partial\omega/\partial k = v_g(\omega(k), U(x))$ in the geometrical optics approximation, where v_g is the group velocity namely the derivative of the dispersion relation including the water current [28,51]. Following Farrell and Watterson [51], since the total group velocity $v_g = U + C_g = \partial\omega/\partial k$ vanishes at

the blocking points, both $dk/dx = (-k\partial U/\partial x)/v_g$ (where C_g is the wave group velocity) and the wave amplitude become infinite and the ray theory breaks down (we recall that the energy of gravity waves scales as the square of the amplitude [52]): in the Appendices, we discuss the prediction of the ray theory as well as the wave theory which smoothes the related divergence to predict the wave envelope.

We plot in Fig. 3 one theoretical ray trajectory in the corresponding space-time diagram where twice the double-bouncing behavior is observed to occur in each white and black hole regions in the (reverse) wormhole travel. As recalled for the Badulin, Pokazeev and Rozenberg experiments [49], the incoming wave I is reflected in a blue-shifted wave B at the white hole horizon. Then, the blueshifted wave B is reflected at the blue horizon and converted into a capillary wave C which enters into the wormhole region in between the white and black horizon. Contrary to the experiments of Badulin, Pokazeev and Rozenberg [49], the capillary wave C which is damped by viscosity is seen to reach the red horizon where it is converted into a longer gravity wave (the redshifted wave R dual to the B wave) and is converted back to an even longer gravity wave T at the black horizon where it is transmitted on the other side of the obstacle.

FIG. 4. Experimental space-time diagrams filtered at the frequency of the incoming wave I (the width of the observation window is roughly 1.1 m and the duration is 7 s). The color scales represent the amplitude in micrometers where we have been forced to adapt the range in three relevant zones for visualization purposes because of the huge viscous damping of the wave amplitudes.

We applied a filter around the sent frequency to clean the noise and visualize only the wave generated by the wave maker and its converted modes at the same frequency (see the space-time diagram of Fig. 4 and the rescaled water depth variations at a given time in Fig. 5). We clearly see the conversion—incident gravity wave I to capillary wave C and capillary wave C to transmitted gravity wave T (from the right to the left)—as well as the interference zones generated by the exponential tail of the Airy pattern [27] (itself due to the interference between the I and B modes) with the capillary waves in both the white and black hole
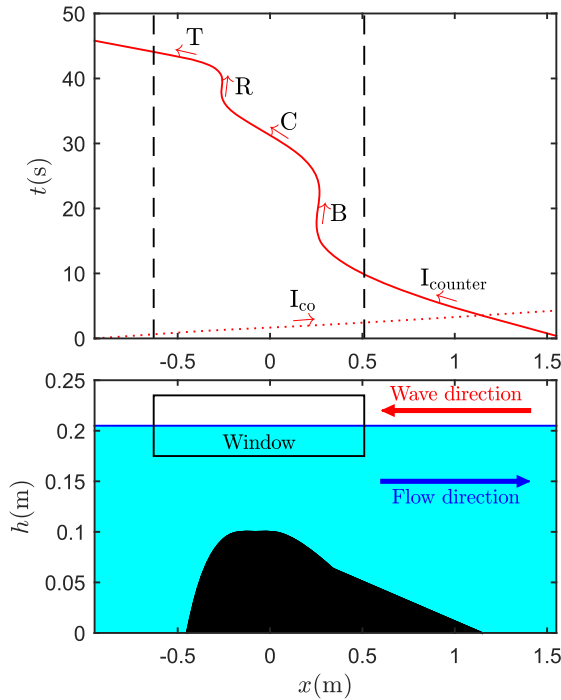

FIG. 3. Bottom: The window studied in the experiments over the obstacle. Top: Scheme of the four different conversions; the red curves represent the theoretical ray trajectories (continuous line, reverse travel from the white horizon to the black one; dashed line, direct travel from the black horizon to the white one) and the vertical black dashed lines correspond to the boundaries of the former window.
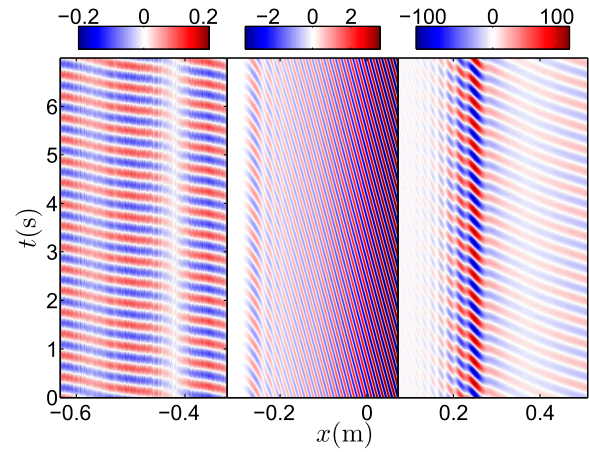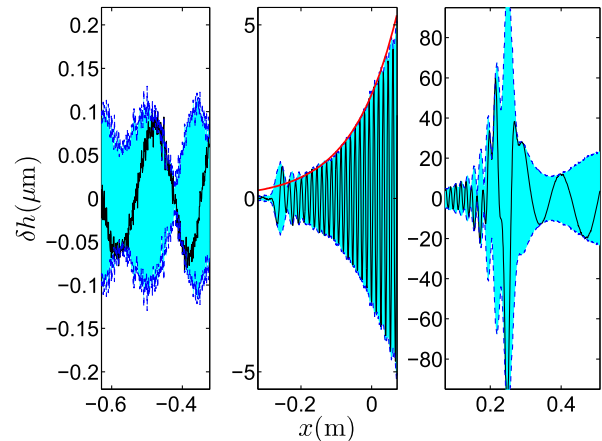

FIG. 5. The black curves show the free surface fluctuations $\delta h(\omega_I, x)$ filtered at the frequency $\omega_I = 14.17$ Hz of the incoming wave I at a fixed time, the blue dashed curves is the experimental envelope and the theoretical red one in the central window represents the exponential damping by viscosity in the capillary regime within the wormhole.

regions (around $x = -0.25$ m and $x = 0.2$ m, respectively) in Fig. 4. These interference patterns are computed theoretically in the Appendices and fit quite well with the interface extraction data.

The enormous damping [53] of the capillary wave C within the wormhole tunnel (see the red curve in the central graphic of Fig. 5) due to the viscous process in the bulk is modeled by the following spatial evolution for its amplitude a_c: $a_c(x) = a_{0c}e^{(-(x-x_0)/L_d)}$ with $a_{0c} = 3$ μm the experimentally measured amplitude at $x_0 = 0$ m on the top of the obstacle (see Fig. 3). The procedure used to remove the exponential damping due to the dissipation is discussed in the Appendices. The related dissipative length inferred from the measurements $L_d = 0.125$ m is shorter than the interhorizon distance L_{wormhole} (black and white) which is close to $0.5\text{m} \simeq 4L_d$: the viscous dissipation takes place but is not sufficient to kill completely the waves in the wormhole tunnel since the extraction method of the water fluctuations is still able to detect them [54]. Even though $L_d < L_{\text{wormhole}}$, still L_{wormhole}/L_d is not yet large enough for the outgoing waves to be beyond the sensitivity of the measuring apparatus.

IV. LINEARITY AND ABSENCE OF HARMONIC GENERATION AND WAVE BREAKING

We plot in Fig. 6 the spatial spectrogram along the water channel namely the evolution of the wave amplitude as a function of the angular frequency and the longitudinal position x, divided by the amplitude of the incident wave at frequency ω_I [37]. We observe that the frequency is conserved with no harmonic generation (at twice the frequency of the wave maker for example). Hence, there is no generation of so-called free harmonics which are solutions of the dispersion relation as can be checked in Fig. 11 of Appendix A. In the same vein, we verified that bounded harmonics $\grave{a}$ la Stokes such as $[2\omega, 2k]$ (which are not solutions of the dispersion relation) are not generated either.

Because the dimensionless water depth kh is always large enough (with a minimum of $kh = 6$) to consider the waves in the deep water regime, the only parameter seizing the effect of the nonlinearity is the camber ka. As discussed in any textbook on water waves, the threshold on the camber ka for the appearance of bounded harmonics is

$$(ka)_{\text{Stokes}} = 0.196 \tanh(kh) \simeq 0.196, \quad kh \gg 1. \quad (1)$$

The range of camber of finite-amplitude capillary waves is not attained as well and we can safely assumed that the experiment is within the linear infinitesimal amplitude approximation (with an error less than 2.5%) without any modification of the wave frequency by the viscosity as discussed by Denner, Paré, and Zaleski [55]:
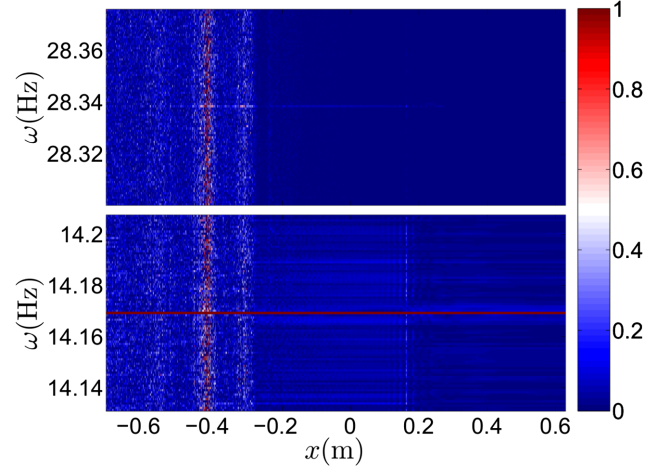

FIG. 6. Spatial spectrogram $\delta h(\omega, x)$ of the dimensionless amplitude evolution relative to the incident wave $\delta h(\omega_I, x)$ showing that the incident frequency ($\omega_I = 14.17$ Hz) is conserved and the amplitude of the first harmonic frequency ($2\omega_I = 28.34$ Hz) is negligible. Higher harmonics are not displayed since they are absent.

$$(ka)_{\text{Viscous}} \simeq 0.314. \quad (2)$$

Similarly, the camber of a typical wave breaking is not reached either:

$$(ka)_{\text{Breaking}} = 0.446 \tanh(kh) \simeq 0.446, \quad kh \gg 1. \quad (3)$$

To obtain the camber we use two methods, the first one by a detection of the crests and troughs providing access to the wavelength and the amplitude as a function of the spatial position x. For the second method, we consider the maximum (in time) of the spatial derivative of the free surface fluctuations. If we consider that these fluctuations are due to a wave whose expression is

$$h(x, t) = a(x) \exp[i(k(x)x - \omega_I t + \phi(x, t))] \quad (4)$$

from which we derive

$$\frac{\partial h}{\partial x} \approx ka \exp\left[i\left(kx - \omega_I t + \phi + \frac{\pi}{2}\right)\right]$$

provided $\frac{\partial k}{\partial x} \ll ka$ and $\frac{\partial a}{\partial x} \ll ka$ (ray approximation), we get an estimation of the camber:

$$\max\left(\left|\frac{\partial h}{\partial x}\right|\right) \approx ka. \quad (5)$$

We plot in Fig. 7 the experimental value of the camber ka using both methods. We show that the camber is always 6 times smaller than the threshold for the appearance of bounded harmonics in particular.
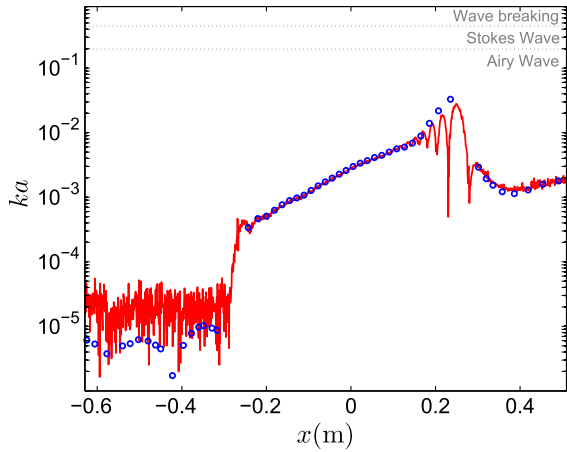
FIG. 7. Experimental value of the camber ka as a function of the spatial position using the extrema detection method (blue circles) and the maximum derivative of the free surface fluctuations method (red line). The horizontal dashed lines indicates the threshold for the appearance of bounded harmonics $(ka)_{Stokes} \simeq 0.196$ and the camber for the wave breaking $(ka)_{Breaking} \simeq 0.446$ in deep water.

V. PHASE SPACE

Badulin, Pokazeev and Rozenberg [49] looked to the space evolution of the wavelength (phase space diagram) of the incoming wave and the converted modes. They saw clearly the double-bouncing behavior as their physical parameters were designed to observe it. Here, as explained in [54], we focus on the (reverse) wormhole travel rather than the double bouncing; hence the optimal regime to observe the travel is such that the distance between the white and blue horizons is small and does not allow one to display the double bouncing as clearly as in Badulin, Pokazeev and Rozenberg work to which we refer the reader [49]. On the contrary, we observe the conversion to the capillary waves and the huge decreases in wavelength in Fig. 8.

We add on the latter graphics, in addition to the obstacle geometry and the local water depth, the two dispersive scales controlling the blocking at the different horizons. As we are mostly in the deep water approximation $kh \gg 1$, the water depth does not play a role in the conversions. For the white and black horizons, the relevant scale is the wavelength at blocking $\lambda^* = (cT)^2/(8\pi h) = gT^2/(8\pi)$ (with $c = \sqrt{gh}$) as explained in [27]. When the wavelength matches this dispersive scale (see Fig. 8), the flow velocity is equal in modulus to the corresponding dispersive group velocity C_g of the waves, namely $U_g = -c^2T/(8\pi h) = -gT/(8\pi)$ for the gravity regime [27] in the deep water approximation. For the blue and red horizons, the dispersive scale is the order of magnitude of the capillary length $l_c = \sqrt{\gamma g/\rho} (= 1.7$ mm in water) as discussed in [28,32]: more precisely, it is the capillary wavelength $\lambda_c = 2\pi l_c (= 1.7$ cm in water) obtained by looking at the
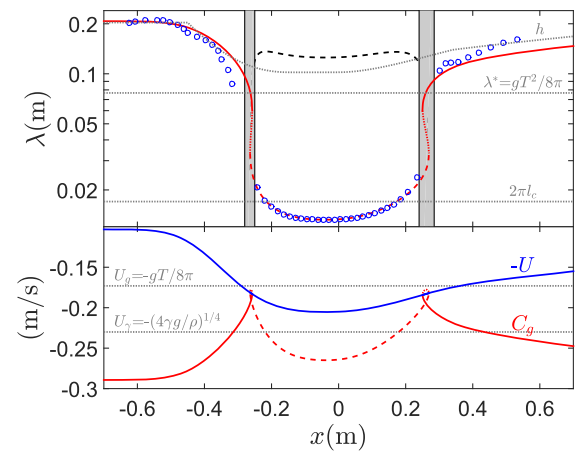

FIG. 8. (Top) Space evolution of the wavelength when reading from right to left. The red line is the theoretical prediction. The blue open dots are the experimental data. The dashed black line is the theoretical dissipative length L_d. The dotted gray lines are the theoretical scales h, λ^* and $\lambda_c = 2\pi l_c$. (Bottom) Spatial evolutions of the velocities of both the flow in blue and the waves in red. In gray, the theoretical blocking velocity for the gravity regime U_g and the threshold for the zero mode appearance U_γ regime which is not reached by the experimental flow speed $U(x)$.

minimum of the phase velocity as a function of the wavelength which is controlling the undulatory properties of the capillary waves regime. Within the wormhole (in between the blue and red horizons), the theory discussed in [28] allows one to derive the wavelength as a function of the speed by canceling the gravity constant $(g = 0)$ in the dispersion relation (a detailed derivation of the wave-current interaction in the pure capillary case will be reported elsewhere since it is lacking in the literature). The dissipative length is of the order of a few wavelengths
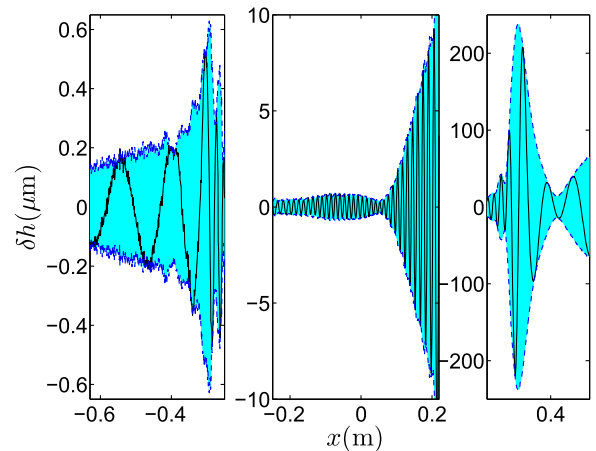

FIG. 9. Direct penetration scenario: the black curves show the free surface fluctuations $\delta h(\omega_{M-T}, x)$ filtered at the frequency $\omega_{M-T} = 16.37$ Hz of the incoming wave I at a fixed time; the blue dashed curves is the experimental envelope.

only in the wormhole tunnel, namely in the capillary regime, whereas it is far bigger in the gravity regime outside of the wormhole and is not represented in Fig. 8.

VI. MORRIS-THORNE WORMHOLE

For completeness and as discussed in [28,32], there is a direct penetration (without double bouncing) with a continuous blueshifting for incoming waves for an incoming period $T_{M-T} = 0.383s < T_c = 0.425s$. This case may be linked to the Morris-Thorne wormhole proposal in general relativity since there is an absence of a horizon (white and black). We confirm the qualitative visual observation of the direct penetration first reported in our previous work [32] by our new quantitative measurements within the linear regime (see Fig. 9) .

VII. CONCLUSION

Can we come back from an interstellar travel after having plunged into a wormhole from the black hole side? Hydraulic traps for the water waves can be linked to hydraulic fountains thanks a tunnel-like region. In hydrodynamics, water waves which enter a black hydraulic horizon emerge from a white hydraulic horizon and do not meet singularities in the flow field (a fact well known for rotating black holes like the Kerr solution which allows wormhole travel via a path that gets around the ring singularities from one universe to another). The travel back has been demonstrated in this work for a hydraulic wormhole using water waves and for the first time in any analogue gravity experiment. Does the singularity exist in reality or is it smoothed by a regularizing process in astrophysics? In nature, waterfalls may either plunge into a body of water and the flow smoothly slows down, or crash on stones which is a more singular fate. We do not know what is inside a gravitational black hole. We do not know if white holes do exist or not in the Universe despite their reality in the kitchen sink (the circular jump). We do not know if cosmological wormholes are science-fiction objects. This paper has tried to nurture our thoughts by using an analogy and maybe humanity will have the chance to travel among stars similarly to gravity-capillary waves surfing on flowing water.

APPENDIX A: CORRELATIONS

To verify that the long gravity wave measured upstream from the obstacle and equally that the capillary wave observed on the top of the obstacle both come from the incoming wave sent downstream, we use a two-point cross-correlation function between a window i and a window j (see Figs. 10 and 11) that was employed recently to measure the spontaneous Hawking radiation at a white hole horizon [37]:

$$G_2^{(i,j)}(\omega; k, k') = |\langle \delta\tilde{h}^{(i)}(\omega, k)\delta\tilde{h}^{(j)}(\omega, k')^* \rangle|. \quad (A1)$$

We consider that the sign of the wave number is positive for the incoming wave propagating in the $-x$ direction.

We decide to separate the three cameras to have three distinct windows where the water depth and the velocity are constant (upstream from the obstacle, on the top of the obstacle and downstream from the obstacle; see Fig. 10).

Because the amplitudes of the waves are very small (they may be inferior to 0.1 μm), we remove the noise in the result. First, in order to suppress the stochastic noise produced by the turbulent flow, we divide the data into 64 equal time intervals and we calculate the average of their Fourier transform. Then, to suppress the noise intrinsic to the experiment (due to either the pump vibration which may induces a global oscillation of the free surface on the total length of the water channel or any other external perturbations), we apply the same procedure to a case without an incoming wave and we subtract this determinist noise to the previous result (see Fig. 11):

$$\delta\tilde{h}(\omega, k) = \langle |\delta\tilde{h}_{\text{wave}}(\omega, k)| \rangle - \langle |\delta\tilde{h}_{\text{no wave}}(\omega, k)| \rangle. \quad (A2)$$

We verify easily in Fig. 11 that the incoming/capillary/transmitted wave is a solution of the dispersion relation in
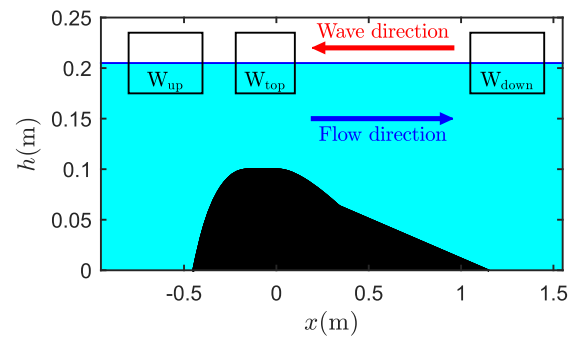

FIG. 10. The studied windows: upstream from the obstacle (W_{up}), on the top of the obstacle (W_{top}), downstream from the obstacle (W_{down}).
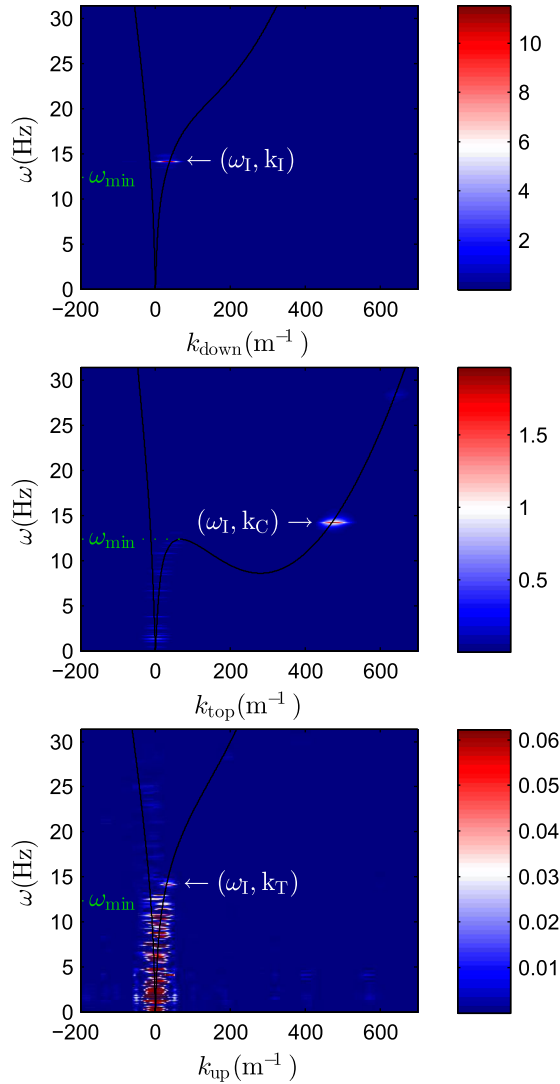
FIG. 11.   Two-dimensional Fourier transforms of the free surface fluctuations $\delta \tilde{h}^{(i)}(\omega, k)$ for each i window [obtained with Eq. (A2)]. Top: Downstream from the obstacle. Center: On the top of the obstacle. Bottom: Upstream from the obstacle. The amplitudes are in microns.

the downstream/top/upstream region. In the upstream region of Fig. 11 (bottom) we observe long gravity waves which are not blocked downstream because their frequencies are smaller than ω_{min} and their amplitudes are of the order of the transmitted wave amplitude which has suffered from viscous damping. Despite our noise-removing procedure, we are unable to cancel them but fortunately we can still isolate the incoming frequency which is slightly superior to ω_{min}. In the downstream region, these waves are also present albeit we do not see them in Fig. 11 (top) because their amplitudes are much smaller than the one of the incoming wave.

We underline that Fig. 11 (top) allows us to extract the initial incoming amplitude before the obstacle in the window W_{down}. From the spatial Fourier transform at

$\omega_I = 14.17$ Hz, we find from the peak in the Fourier space its maximum which will be considered as our initial incoming amplitude $a_0 = 11.53$ μm.

To quantify the strength of the correlations, we compute

$$g_2^{(i,j)}(\omega; k_a, k_b) = \frac{G_2^{(i,j)}(\omega; k_a, k_b)}{\sqrt{G_2^{(i,i)}(\omega; k_a, k_a) G_2^{(j,j)}(\omega; k_b, k_b)}}.$$

$$(A3)$$

We obtain for the cross correlation between the incident wave end the capillary wave a correlation strength of $g_2^{(down,top)}(\omega_i; k_I, k_C) = 85.11\%$, between the capillary wave and the transmitted wave $g_2^{(top,up)}(\omega_i; k_C, k_T) = 94.43\%$ and between the transmitted and the incident wave $g_2^{(up,down)}(\omega_i; k_T, k_I) = 80.98\%$.
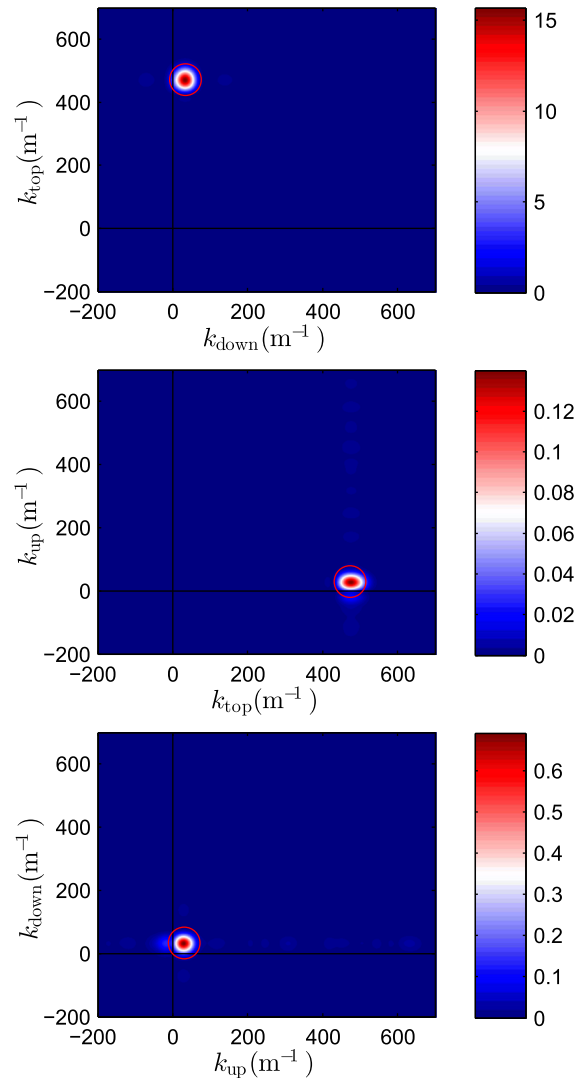

FIG. 12.   Cross-correlation function $G_2^{(i,j)}(\omega; k, k')$ for each couple of windows (i, j). Top: (d, t) couple. Center: (t, u) couple. Bottom: (u, d) couple. The amplitudes are in μm^2.

For completeness, we plot the correlation maps $G_2^{(i,j)}(\omega; k, k')$ in the (k, k') wave-vector plane for each region in Fig. 12 [37] and we check that the experimental correlation peaks coincide with the theoretical prediction for each couple of wave vectors (symbolized by the red circles).
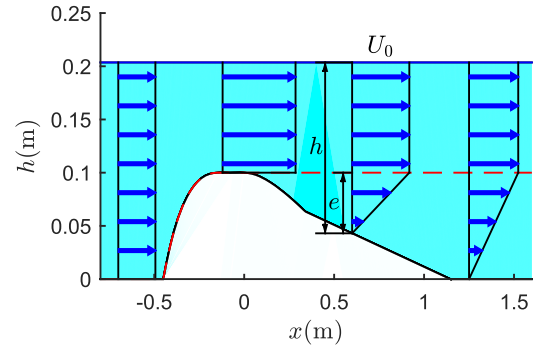

FIG. 13. Model representing the development of the boundary layer in the descending part of the obstacle. The red dashed curve corresponds to the thickness of the boundary layer (e).

APPENDIX B: THEORETICAL ESTIMATION OF THE AMPLITUDE EVOLUTION CONSIDERING THE WAVE ACTION CONSERVATION AND THE DISSIPATION

First, we need to estimate the flow over the obstacle to know the parameters like $U(x)$ involved in the dispersion relation at each space position x. Past velocity measurements (not reported here) over the same obstacle but with different flow configurations (flow rate and water depth) have shown that a boundary layer is created in the downstream part due to the descending slope of the obstacle. The position of the boundary layer where it matches the uniform flow seems to be approximatively equal to the maximum height of the obstacle. This boundary layer modifies the velocity at the free surface (due to the flow rate conservation) and we need to take into account the effect of vorticity in the dispersion relation.

We base our reasoning to estimate the spatial evolution of the free surface on an analytical resolution of the dispersion relation for surface wave propagation on a shear flow with constant vorticity (see details in [35]):

$$\omega = -\left(U_0 k - \frac{\alpha}{2}\tanh(kh)\right)$$
$$+ \sqrt{\left(\frac{\alpha}{2}\tanh(kh)\right)^2 + \left(gk + \frac{\gamma}{\rho}k^3\right)\tanh(kh)}, \quad \text{(B1)}$$

where $U_0 > 0$ is the current speed at the free surface flowing in the $+x$ direction, $\alpha = U_0/h$ the parameter characterizing the flow vorticity, $\gamma = 73 \times 10^{-3}$ N/m the surface tension and $\rho = 10^3$ kg/m³ the density of water.

In our case the vertical velocity profile is not linear so we apply a simplified model to approximate the vertical flow profile where the latter is linear from the bottom (or obstacle) to the boundary layer limit and constant from the boundary layer limit to the free surface (see Fig. 13). With this assumption, we correct the parameter characterizing the flow vorticity by a coefficient equal to the thickness of the boundary layer ($\alpha = RU_0/h$ with the ratio $R = e/h$). Moreover, we can express the surface velocity as a function of the experimentally imposed flow rate $U_0 = (Q/Wh)(1 - R/2)^{-1}$.

According to Bretherton and Garrett [56], the quantity conserved in a wave-current interaction process is the wave action density $\mathcal{A}' = E'/\omega'$ with $E' = \frac{1}{2}a^2(\rho g + \gamma k^2)$ the wave energy density and ω' the relative frequency both in

the flow frame denoted by a prime (the wave energy density is not conserved since the waves exchange energy with the spatially varying flow). This conservation leads to a constant wave action flux for all space positions x (assuming stationarity) written as

$$J = \frac{1}{2}a^2(\rho g + \gamma k^2)\frac{v_g}{\omega'} \sim a^2(1 + l_c^2 k^2)\frac{v_g}{\omega'} \quad \text{(B2)}$$

with $J = \mathcal{A}'v_g$ the wave action flux, a the wave amplitude, ρ the water density and $l_c = \sqrt{\gamma/(\rho g)}$ the capillary length. The group velocity in the laboratory frame v_g, the relative frequency in the flow frame ω' and the wave number k are given in each position x by the dispersion relation (B1). Equation (B2) allows one to compute the evolution of the wave amplitude when the flow varies in a nondissipative regime. We underline forcefully that we use here the expression of the wave action density assuming no vorticity. The latter enters into the dispersion relation and the group velocity in order to compute the conservation of wave action flux. This approximation is sufficient at our level. An exact expression for the wave action density for a linear shear profile was derived by Jonsson, Brink-Kjaer, and Thomas in 1978 but it implies some complications that we avoid in our simple estimation [57]. In particular, the converted waves such as the capillary waves have a wavelength smaller than $(h - e)$ so we can assume that they "feel" a uniform vertical velocity profile.

As we have been forced to rescale the amplitude scales in three separate windows to display the decrease of the wave amplitude during the propagation and thanks to the knowledge of the exponential damping [53,54], we can remove the latter and show our results cleaned from the effect of viscosity in Fig. 14, where we plot both a free surface variation at a given time within the undamped envelope (top) as well as a three-dimensional space-time diagram with the same vertical scale (bottom).

To take into account the effect of exponential dissipation of the wave amplitude, we introduce the dissipative length
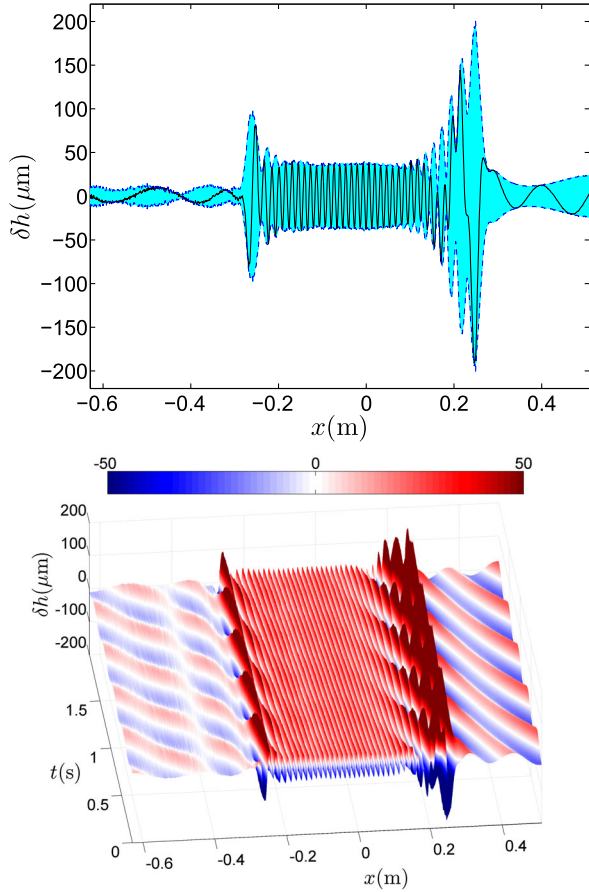
FIG. 14.   (Top) Free surface variations $\delta h(\omega_I, x)$ at a given time with its corresponding envelope for the fixed frequency of the incoming wave ω_I; (bottom) three-dimensional space-time diagram with a fixed vertical scale for the amplitude variations. For both graphics, viscous dissipation was removed to have the same vertical scale.

based on the Lamb formula (see an extensive discussion on the effect of dissipation in the context of analogue gravity in [54]):

$$L_d = \frac{v_g}{2\nu k^2}, \qquad (B3)$$

where $\nu = 1.05 \times 10^{-6}$ m^2/s is the viscosity of pure water at 18 °C. We assume that the fluorescent dye we used namely fluoresceine does not modify too much the value of viscosity.

In the wormhole tunnel, the capillary wave envelope is constant. Before the tunnel (on the right in Fig. 14), one observes an interference modulation of the envelope due to the existence of the transverse mode due to finite width of the channel. After the tunnel (on the left in Fig. 14), one also sees another interference modulation of the envelope due to the reflection on the wall of the transmitted wave T at the end of the water channel because of its finite length.

Combining the conservation of the wave action density [Eq. (B2)] and an exponential decrease due to the dissipation [considering the dissipative length (B3)], we can compute the "geometrical optics" evolution of the amplitude starting from the initial amplitude $a_0 = 11.53$ μm on the downstream part (at the right of the obstacle) before the wormhole travel:

$$\frac{a_{(i+1)}}{a_{(i)}} = \sqrt{\frac{|v_g(k_{(i)})|}{|v_g(k_{(i+1)})|} \frac{\omega'(k_{(i+1)})}{\omega'(k_{(i)})} \frac{1 + l_c^2 k_{(i)}^2}{1 + l_c^2 k_{(i+1)}^2}} e^{-|\delta x|/L_{d(i)}}.$$

$$(B4)$$

The subscript (i) corresponds to the variable taken at a spatial position x, and $(i + 1)$ at $x + \delta x$. The sign of δx depends of the propagation direction of the solution. Figure 15 shows a fairly good agreement between the geometrical solution obtained with Eq. (B4) and the experimental results; the differences may come from the hypotheses about the model of the velocity profile, the expression of the energy or the dispersion relation in the presence of vorticity.

We also see in Fig. 15 some undulations in the envelope: for example, between $x = -0.63$ m and $x = -0.28$ m. Those interferences come from other waves existing in the experiment. We will try to identify these waves, separating four distinct zones of interferences:

zone 1: before the first conversion (from $x = 0.27$ m to $x = 0.50$ m),

zone 2: after the first double bouncing (from $x = 0.09$ m to $x = 0.25$ m),

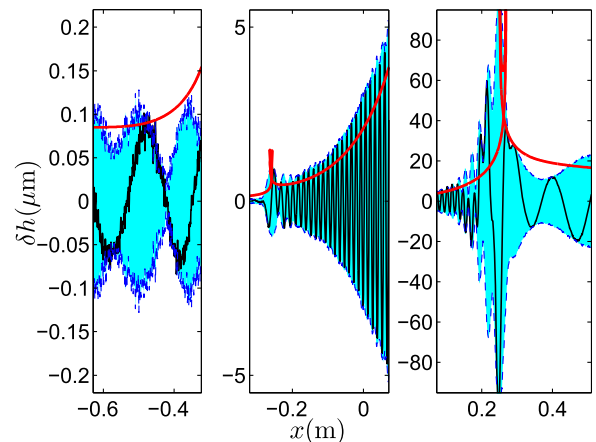zone 3: before the second double bouncing (from $x = -0.25$ m to $x = -0.16$ m),

FIG. 15.   The black curve shows the spatial evolution of the free surface fluctuations filtered at the frequency of the incoming wave for a given time, the blue dashed curves is the envelope $\delta h(\omega_I, x)$ and the red curve is the result of the geometrical optics calculation based on Eq. (B4).
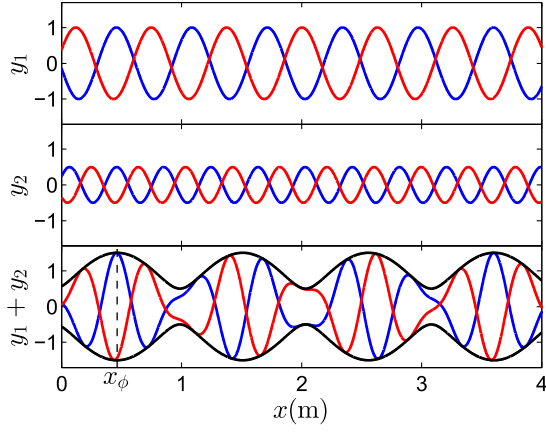
FIG. 16. Example of a two wave interference with $y_i = a_i \cos(k_i x - \omega t - \phi_i)$, $\omega = 1$ Hz; the blue curves correspond to $t = 1.5$ s and the red one to $t = 4.4$ s. Top: First wave ($i = 1$) with $a_1 = 1$ (dimensionless amplitude), $k_1 = 10$ m^{-1} and $\phi_1 = 3.2$. Center: Second wave ($i = 2$) with $a_2 = 0.5$, $k_2 = 16$ m^{-1} and $\phi_2 = 6.7$. Bottom: Wave superposition; the black curves indicate the spatial envelope A_2 (and $-A_2$) of the interference pattern with $x_\phi = 0.463$ m.

zone 4: after all conversions (from $x = -0.63$ m to $x = -0.28$ m).

To deduce this interferences, we use the general formula of the spatial envelope A_n of the interference pattern of n waves:

$$A_n = \left(\sum_{i=1}^{n} \sum_{j=1}^{n} a_i a_j \cos((k_i - k_j)x - (\phi_i - \phi_j)) \right)^{1/2},$$

(B5)

where ϕ_i is the phase shift and k_i the wave number of the mode i with amplitude a_i. a_i, k_i and ϕ_i can depend on the space position x.

For the peculiar case where there are only two waves involved, Eq. (B5) can be reduced to

$$A_2 = (a_1^2 + a_2^2 + 2a_1 a_2 \cos((k_1 - k_2)x - (\phi_1 - \phi_2)))^{1/2}$$

(B6)

and the phase shift difference of the interference pattern can be written $\phi_1 - \phi_2 = (k_1 - k_2)x_\phi$, where x_ϕ is one of the maxima of the interference pattern. Figure 16 shows an example of a two wave interference.

Zone 1 (Fig. 17 right).—The interference in the region where an oscillation around the amplitude of the incident wave is observed could be explained by the superposition of the latter with a transverse mode. Since we need to take into account the vorticity in this region, we suppose that the dispersion relation for waves with two components—longitudinal and tranverse—projected on $\vec{x}$ is

$$\omega = -\left(U_0 k_x - \frac{\alpha}{2} \frac{k_x}{k} \tanh(k) \right)$$
$$+ \sqrt{\left(\frac{\alpha}{2} \frac{k_x}{k} \tanh(k) \right)^2 + \left(gk + \frac{\gamma}{\rho} k^3 \right) \tanh(k)} \quad \text{(B7)}$$

with $k = \sqrt{k_x^2 + k_y^2}$. Previously, we have considered waves with only a longitudinal component $k = k_x$ and $k_y = 0$. In this case, because of the finite width of the water channel, we have a quantization of the transverse component with $k_y = (n\pi/W)$ ($n \in \mathbb{N}$ and W is the width of the water channel).

The measurement is done in the center of the channel, so only half of the transverse modes are taken into account ($n \in 2\mathbb{N}$). We check theoretically that the only even mode existing for the incoming frequency is $n = 2$.

By assuming arbitrarily that the amplitude of the transverse component k_y is equal to half the one of the
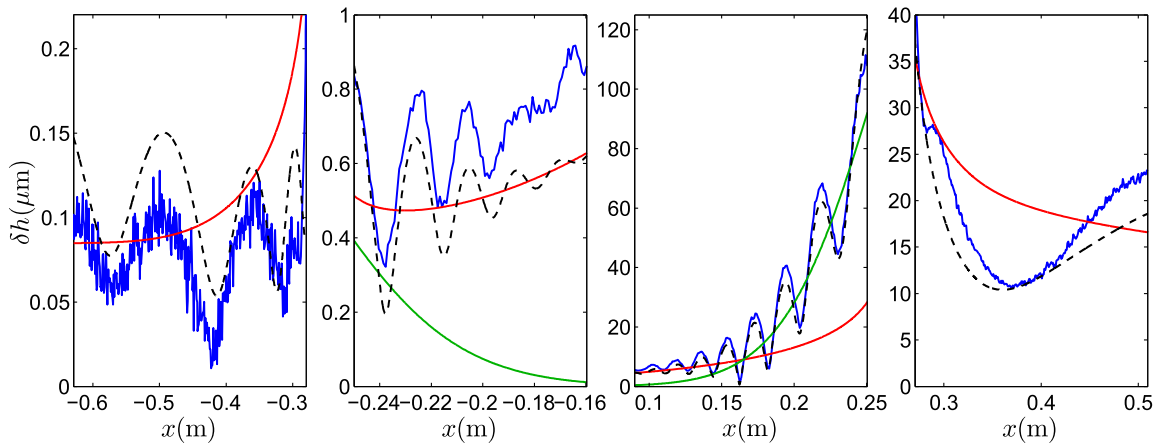

FIG. 17. Experimental envelope (blue line), geometrical solution (red line), Airy tails (green line) and interference fits (black dashed line).

longitudinal component k_x, we recover our experimental results with a corresponding fitting curve. This strong hypothesis relies on our visual observations of the free surface with the interference patterns between the longitudinal and transverse components over the obstacle in the probed window.

Knowing the amplitude of the two waves and their wave numbers, we apply Eq. (B6) where x_ϕ is an arbitrary maximum of interference read directly on the envelope $\delta h(\omega_I, x)$ in zone 1.

Zone 2 (Fig. 17 center right).—*Prima facie*, there is only the capillary wave if we consider the geometrical solution using Eq. (B4) but we need to consider that, when the incident wave is converted into a blueshifted wave (at the white horizon), the amplitude of this double solution does not go to zero immediately after the horizon but decreases on a certain distance. This looks like an Airy function [27], at least for the decreasing part (we are not interested in the oscillating part of the Airy function since the distance between the white and blue horizons is shorter than one local wavelength). We compute an Airy function $a_* \mathrm{Ai}(X)$, where $-X = (x - x_*)/L_s$ (we put a minus sign before X because the decreasing part of the Airy function is defined for $x > x_*$ and in this case, it is observed for $x < x_*$), x_* is the position the blocking point, L_s is the stopping length and a_* the amplitude at x_* [32]. The stopping length can be calculating with different formulas, for example the one introduced by Trulsen and Mei in 1993 [32,50]:

$$L_s = \left(\frac{U_*^2}{2 k_* \omega \left(\frac{\partial U}{\partial x} \right)_{x_*}} \right)^{1/3}, \qquad (B8)$$

where U_* is the velocity, k_* the wave number, and $\left(\frac{\partial U}{\partial x} \right)_{x_*}$ the velocity gradient, all taken at the blocking point x_*.

We found in our case for the white horizon (from incident to blueshifted waves) $Ls = 0.0427$ m. Then, we use Eq. (B5) to deduce the envelope.

Zone 3 (Fig. 17 center left).—We applied the same procedure as in the second zone; we have, on one hand, the capillary wave and, on the other hand, the tail of the Airy function due to the conversion from the redshifted to the transmitted waves. In this case, $X = (x - x_*)/L_s$ and the stopping length [using Eq. (B8)] is found to be $L_s = 0.0340$ m.

Zone 4 (Fig. 17 left).—Because the water tank is not infinitely long, the transmitted wave is reflected by the end wall in the convergent part of the water channel (see Fig. 1). The amplitude of this reflected wave can be calculated with Eq. (B4) (considering that all of the wave action density is reflected). In our case, this amplitude is about half the transmitted amplitude. Considering also the transverse mode, in the same way as zone 1, we obtain an interference between three waves again.

The geometrical solution [calculated with Eq. (B4), called in the next a_v^{th}] matches with the experimental result, and we can obtain another geometrical solution (called in the next a_{nv}^{th}) where the exponential term in Eq. (B4) is removed to stay in a nondissipative regime. Then, we can redress our experimental result using

$$a_{nv}^{\exp}(x) = a_v^{\exp}(x) \frac{a_{nv}^{th}(x)}{a_v^{th}(x)}. \qquad (B9)$$

This procedure allows to see more clearly in Fig. 14 the conversion from long to capillary waves within the white hole region and from capillary to long waves on the other side of the wormhole within the black hole region.

There is a lot of estimation in this method (simplified model for the velocity field, dispersion relation including vorticity, Airy function, interference pattern, etc.) but the quite good superposition of this theoretical estimation and the experimental results confirm its validity. A velocity field measurement of the flow over the obstacle would be necessary to verify our estimations but it is outside the scope of this study.

[1] J. Eisenstaedt, in *Einstein and the History of General Relativity, Proceedings of the 1986 Osgood Hill Conference*, Einstein Studies Vol. 1, edited by J. Stachel and Don Howard (Birkhäuser, Boston, 1989), pp. 213–233.

[2] K. Schwarzschild, Über das Gravitationsfeld eines Massenpunktes nach der Einsteinschen Theorie, Sitzungsber. K. Preuss. Akad. Wiss., **7**, 189 (1916) .

[3] A. Einstein and N. Rosen, The Particle Problem in the General Theory of Relativity, Phys. Rev. **48**, 73 (1935).

[4] L. Flamm, Comments on Einstein's theory of gravity, Phys. Z. **17**, 448 (1916).

[5] M. Visser, *Lorentzian Wormholes: From Einstein to Hawking* (American Institute of Physics, New York, 1995).

[6] *Wormholes, Warp Drives and Energy Conditions*, Fondamental Theories of Physics Vol. 189, edited by F. S. Lobo (Springer, New York, 2017).

[7] C. W. Misner and J. A. Wheeler, Classical physics as geometry, Ann. Phys. (N.Y.) **2**, 525 (1957).

[8] J. A. Wheeler, On the nature of quantum geometrodynamics, Ann. Phys. (N.Y.) **2**, 604 (1957).

[9] J. A. Wheeler, *Geometrodynamics* (Academic, New York, 1962), Vol. 1.

[10] R. W. Fuller and J. A. Wheeler, Causality and Multiply-Connected Space-Time, Phys. Rev. **128**, 919 (1962).

[11] H. G. Ellis, Ether flow through a drainhole: A particle model in general relativity, J. Math. Phys. (N.Y.) **14**, 104 (1973); Erratum, J. Math. Phys. (N.Y.) **15**, 520(E) (1974).

[12] R. W. White, Acoustic ray tracing in moving inhomogeneous fluids, J. Acoust. Soc. Am. **53**, 1700 (1973).

[13] J. L. Anderson and E. A. Spiegel, Radiative transfer through a flowing refractive medium, Astrophys. J. **202**, 454 (1975).

[14] W. G. Unruh, Experimental Black-Hole Evaporation?, Phys. Rev. Lett. **46**, 1351 (1981).

[15] W. G. Unruh, in *Quantum Analogues: From Phase Transitions to Black Holes and Cosmology* (Springer, Berlin, 2007), pp. 1–4.

[16] C. Barcelo, S. Liberati, and M. Visser, Analogue gravity, Living Rev. Relativ. **8**, 12 (2011).

[17] S. J. Robertson, The theory of Hawking radiation in laboratory analogues, J. Phys. B **45**, 163001 (2012).

[18] D. Faccio, F. Belgiorno, S. Cacciatori, V. Gorini, S. Liberati, and U. Moschella, *Analogue Gravity Phenomenology: Analogue Spacetimes and Horizons, from Theory to Experiment*, Lect. Notes Phys. (Springer, New York, 2013).

[19] S. W. Hawking, Black hole explosions, Nature (London) **248**, 30 (1974).

[20] T. Jacobson, Black hole evaporation and ultrashort distances, Phys. Rev. D **44**, 1731 (1991).

[21] W. G. Unruh, Sonic analogue of black holes and the effects of high frequencies on black hole evaporation, Phys. Rev. D **51**, 2827 (1995).

[22] T. Jacobson, On the origin of the outgoing black hole modes, Phys. Rev. D **53**, 7082 (1996).

[23] F. Girelli, S. Liberati, and L. Sindoni, Planck-scale modified dispersion relations and Finsler geometry, Phys. Rev. D **75**, 064015 (2007).

[24] S. W. Hawking, Information preservation and weather forecasting for black holes, arXiv:1401.5761.

[25] R. Schützhold and W. G. Unruh, Gravity wave analogues of black holes, Phys. Rev. D **66**, 044019 (2002).

[26] G. Rousseaux, C. Mathis, P. Maïssa, P. Coullet, T. G. Philbin, and U. Leonhardt, Observation of negative phase velocity waves in a water tank: A classical analogue to the Hawking effect?, New J. Phys. **10**, 053015 (2008).

[27] J.-C. Nardin, G. Rousseaux, and P. Coullet, Wave-Current Interaction as a Spatial Dynamical System: Analogies with Rainbow and Black Hole Physics, Phys. Rev. Lett. **102**, 124504 (2009).

[28] G. Rousseaux, P. Maïssa, C. Mathis, P. Coullet, T. G. Philbin, and U. Leonhardt, Horizon effects with surface waves on moving water, New J. Phys. **12**, 095018 (2010).

[29] S. Weinfurtner, E. W. Tedford, M. C. J. Penrice, W. G. Unruh, and G. A. Lawrence, Measurement of Stimulated Hawking Emission in an Analogue System, Phys. Rev. Lett. **106**, 021302 (2011).

[30] G. Jannes, R. Piquet, P. Maissa, C. Mathis, and G. Rousseaux, Experimental demonstration of the supersonic-subsonic bifurcation in the circular jump: A hydrodynamic white hole, Phys. Rev. E **83**, 056312 (2011).

[31] G. Jannes, P. Maissa, T. G. Philbin, and G. Rousseaux, Hawking radiation and the boomerang behavior of massive modes near a horizon, Phys. Rev. D **83**, 104028 (2011).

[32] J. Chaline, G. Jannes, P. Maïssa, and G. Rousseaux, in *Analogue Gravity Phenomenology* (Springer, New York, 2013), pp. 145–165.

[33] G. Rousseaux, D. Uminsky, and R. Levy, in Proceedings of the International Symposium on Turbulence and Shear Flow Phenomena (TSFP8), Poitiers, France, 2013 (unpublished).

[34] L.-P. Euvé, F. Michel, R. Parentani, and G. Rousseaux, Wave blocking and partial transmission in subcritical flows over an obstacle, Phys. Rev. D **91**, 024020 (2015).

[35] P. Maïssa, G. Rousseaux, and Y. Stepanyants, Wave blocking phenomenon of surface waves on a shear flow with a constant vorticity, Phys. Fluids **28**, 032102 (2016).

[36] C. Peloquin, L.-P. Euvé, T. G. Philbin, and G. Rousseaux, Analog wormholes and black hole laser effects in hydrodynamics, Phys. Rev. D **93**, 084032 (2016).

[37] L.-P. Euvé, F. Michel, R. Parentani, T. G. Philbin, and G. Rousseaux, Observation of Noise Correlated by the Hawking Effect in a Water Tank, Phys. Rev. Lett. **117**, 121301 (2016).

[38] T. Torres, S. Patrick, A. Coutant, M. Richartz, E. W. Tedford, and S. Weinfurtner, Observation of superradiance in a vortex flow, Nat. Phys. **13**, 833 (2017).

[39] C. Sabin, Quantum simulation of traversable wormhole spacetimes in a dc-SQUID array, Phys. Rev. D **94**, 081501 (2016).

[40] M. S. Morris, K. S. Thorne, and U. Yurtsever, Wormholes, Time Machines and Weak Energy Condition, Phys. Rev. Lett. **61**, 1446 (1988).

[41] M. Morris and K. Thorne, Wormholes in spacetime and their use for interstellar travel: A tool for teaching general relativity, Am. J. Phys. **56**, 395 (1988).

[42] T. Muller, Exact geometric optics in a Morris-Thorne wormhole spacetime, Phys. Rev. D **77**, 044043 (2008).

[43] A. Doroshkevich, J. Hansen, I. Novikov, and A. Shatskiy, Passage of radiation through wormholes, Int. J. Mod. Phys. D **18**, 1665 (2009).

[44] O. James, E. von Tunzelmann, P. Franklin, and K. S. Thorne, Visualizing interstellar's wormhole, Am. J. Phys. **83**, 486 (2015).

[45] F. S. Lobo, From the Flamm-Einstein-Rosen bridge to the modern renaissance of traversable wormholes, Int. J. Mod. Phys. D **25**, 1630017 (2016).

[46] A. Y. Basovich and V. I. Talanov, Transformation of short surface waves on inhomogeneous currents, Izv. Acad. Sci., USSR, Atmos. Oceanic Phys. (Engl. Transl.) **13**, 514 (1977).

[47] R. Smith, in *Waves on Water of Variable Depth* (Springer, Berlin, 1977), pp. 154–164.

[48] K. V. Pokazeev and A. D. Rozenberg, Laboratory studies of regular gravity-capillary waves in currents, Oceanology (Moscow, Russ. Fed.) **23**, 429 (1983).

[49] S. I. Badulin, K. V. Pokazeev, and A. D. Rozenberg, A laboratory study of the transformation of regular gravity-capillary waves in inhomogeneous flows, Izv. Acad. Sci., USSR, Atmos. Oceanic Phys. (Engl. Transl.) **19**, 782 (1983).

[50] K. Trulsen and C. C. Mei, Double reflection of capillary/gravity waves by a nonuniform current: A boundary-layer theory, J. Fluid Mech. **251**, 239 (1993).

[51] B. Farrell and I. Watterson, Rossby waves in opposing currents, J. Atmos. Sci. **42**, 1746 (1985).

[52] M. W. Dingemans, *Water Wave Propagation over Uneven Bottoms* (World Scientific, Singapore, 1997).

[53] P. H. LeBlond and F. Mainardi, The viscous damping of capillary-gravity waves, Acta Mech. **68**, 203 (1987).

[54] S. Robertson and G. Rousseaux, Viscous dissipation of surface waves and its relevance to analogue gravity experiments, arXiv:1706.05255.

[55] F. Denner, G. Paré, and S. Zaleski, Dispersion and viscous attenuation of capillary waves with finite amplitude, Eur. Phys. J. Spec. Top. **226**, 1229 (2017).

[56] F. P. Bretherton and C. J. R. Garrett, Wavetrains in inhomogeneous moving media, Proc. R. Soc. A **302**, 529 (1968).

[57] I. G. Jonsson, O. Brink-Kjaer, and G. P. Thomas, Wave action and set-down for waves on a shear current, J. Fluid Mech. **87**, 401 (1978).